SPARSITY CONSTRAINED LINEAR TANGENT SPACE ALIGNMENT MODEL (LTSA) FOR 3D CARDIAC EXTRACELLULAR VOLUME MAPPING

Ismaël Mounime, Wonil Lee, Thibault Marin, Paul K. Han, Yanis Djebra, Samira V. Eslahi, Pietro Gori, Elsa Angelini, Georges El Fakhri, Chao Ma

SPARSITY CONSTRAINED LINEAR TANGENT SPACE ALIGNMENT MODEL (LTSA) FOR 3D CARDIAC EXTRACELLULAR VOLUME MAPPING

Ismaël B.G. Mounime[⋆†‡], *Wonil Lee*[⋆‡], *Thibault Marin*[⋆‡], *Paul K. Han*[⋆], *Yanis Djebra*[⋆‡], *Samira V. Eslahi*[⋆], *Pietro Gori*[†], *Elsa Angelini*[†], *Georges El Fakhri*[‡], *Chao Ma*[⋆‡]

[⋆] Massachusetts General Hospital, Harvard Medical School, Boston, MA, USA,
[†] LTCI, Télécom Paris, Institut Polytechnique de Paris, Paris, France,
[‡]Department of Radiology and Biomedical Imaging, Yale School of Medicine, New Haven, CT, USA

ABSTRACT

Cardiac longitudinal relaxation time (T_1) and extracellular volume (ECV) are valuable bio-markers used for the quantitative characterization of cardiac tissue properties, showing great potential in many clinical applications such as diffuse fibrosis. However, cardiac T_1 and ECV mapping is difficult because of respiratory and cardiac motions. A unique challenge for post-contrast T_1 mapping is that the concentration of contrast agent also changes over time. Recently, a linear tangent space alignment (LTSA) model-based fast MRI method has been proposed to enable high-resolution, high-frame-rate dynamic MR with sparsely sampled (k, t)-space data by leveraging the intrinsic low-dimensional manifold structure of dynamic MR images, showing superior performance over the low-rank model-based methods. This work extends the LTSA method by imposing an additional sparsity constraint on the subspace alignment matrix of the LTSA model for improved image reconstruction. The performance of the proposed method is validated in 3D free-breathing, pre- and post-contrast cardiac T_1 mapping as well as ECV mapping using in vivo data acquired on healthy volunteers at 3T.

***Index Terms*—** MR image reconstruction, cardiac T_1 mapping, cardiac extracellular volume mapping, linear tangent space alignment (LTSA), manifold learning

1. INTRODUCTION

Cardiac T_1 mapping is a useful diagnostic tool for detecting cardiac diseases that alter the myocardium tissue composition, such as myocarditis, amyloidosis, or Anderson-Fabry disease [1, 2]. Cardiac T_1 mapping, performed before and after contrast agent injection, enables the quantification of extracellular volume (ECV). This emerging bio-marker is important for diseases such as diffuse fibrosis, a condition particularly challenging to detect using the qualitative late gadolinium enhancement (LGE) [1, 2]. However, cardiac T_1 and ECV mapping is difficult because of respiratory and cardiac motions. A unique challenge for post-contrast T_1 mapping is that the concentration of contrast agent also changes over time. Clinically, cardiac T_1 and ECV mapping are performed using the Modified Look-Locker Inversion recovery (MOLLI) method [3], which is a 2D imaging technique with electrocardiogram (ECG)-gated acquisition during breath holding. Depending on the heart beat rate, the subjects need to hold their breath for more than 10 seconds, imposing a substantial burden on patients especially for multi-slice acquisitions to cover the whole heart. Various efforts have been made to enhance the applicability of MOLLI for multiple 2D slices [4] or 3D [5] cardiac T_1 mapping, leveraging sparse sampling strategies such as Compressed Sensing and Parallel Imaging. These approaches have shown promise in addressing some of the existing challenges associated with cardiac T_1 and ECV mapping but still require breath-holding and/or provide limited spatial coverage and resolution in the slice direction.

Over the past decade, many advanced reconstruction models have been proposed to enable high-resolution artifact-free dynamic images from highly undersampled (k, t)-space data. The Low-Rank model (LR) [6] assumes the (k, t)-space data lie on a low-dimensional subspace, which significantly reduces the number of unknowns in the resultant image reconstruction problem. The LR-based method has been applied to free-breathing 3D joint T_1/B_1^+ mapping of the heart and shown good agreement between the estimated myocardium T_1 values with the MOLLI method in the presence of transmit B_1 inhomogeneities at 3T [7]. This model has been further extended to Local Low-Rank (LLR) model [8, 9], which exploits the local low rank structures adapted to the neighborhood of image patches. Another extension of the LR model, termed multi-scale Low-Rank [10] model, seeks to harness the advantages of both sparse LR and LLR methods, accommodating a broad spectrum of dynamic variations. Methods based on Low-Rank tensor (LRT) decomposition [11] leverage the inherent correlations of high-dimensional multi-array data along multiple directions, e.g., the correlation of the dynamic images along the temporal changes due to respiratory motion, cardiac motion, and T_1 contrast changes, respectively, as in the MR Multitasking method [12, 13] and a patch-based LRT model [14] for cardiac T_1 mapping. Deep learning-based methods [15, 16] have also been developed to reduce the number of heartbeats required in cardiac T_1 mapping with breath-holding acquisitions.

This work presents a 3D free-breathing cardiac ECV mapping method using a Linear Tangent Space Alignment (LTSA) model-based framework for data acquisition and image reconstruction [17]. The LTSA model exploits the intrinsic low-dimensional manifold structure of high-dimensional dynamic MR images via a bi-linear model, which can be considered a nonlinear generalization of the linear LR and LRT model. The LTSA model has been applied to reconstruct high-resolution, high-frame-rate dynamic images from sparsely sampled (k, t)-space, showing superior performance over the state-of-the-art real-time imaging methods. In this study, we extended this method by incorporating an additional sparsity penalty on the alignment matrix of the LTSA model for improved image reconstruction performance. We demonstrated the performance of the proposed method in 3D cardiac ECV mapping on healthy subjects. Specifically, the contributions of this work are:

- Introduce an additional sparsity constraint on the subspace align-

ment matrix to the LTSA model for improved image reconstruction;
- Compare the performance of the sparsity constrained LTSA model against two state-of-the-art methods (i.e., the LTSA method without sparsity constraints on the alignment matrix and the LR+S method);
- Validate the performance of the proposed model in 3D free-breathing, pre- and post-contrast cardiac T_1 and ECV mapping using in vivo data acquired on healthy volunteers at 3T.

2. METHODS

2.1. Linear Tangent Space Alignment (LTSA) model for dynamic MRI

The Linear Tangent Space Alignment (LTSA) model [17, 18] assumes that high-dimensional dynamic MR images lie in a low-dimensional manifold of dimension D:

$$\mathbf{x}_m = f(\boldsymbol{\tau}_m), m = 1, \dots, M \tag{1}$$

where $\mathbf{x}_m \in \mathbb{C}^{N\times 1}$ denotes the temporal signal at voxel m, N the number of time frames, M the number of voxels, $\boldsymbol{\tau}_m \in \mathbb{C}^{D\times 1}$ the corresponding coordinate in the feature space, and f the unknown nonlinear mapping between the feature and input spaces.

The local structure of the underlying manifold is constructed by grouping frames of the dynamic MR images into several neighborhoods based on certain similarity metrics or surrogate signals (e.g., motion navigators or ECG signals). The temporal signals of a voxel at $\boldsymbol{r}_m$ in a neighborhood $q \in \{1, \dots, Q\}$ can be expressed as:

$$\begin{aligned}\mathbf{x}_m^{(q)} =& [x(\boldsymbol{r}_m, t_1^{(q)}), \dots, x(\boldsymbol{r}_m, t_{P_q}^{(q)})]^{\mathrm{T}} \\ =& \boldsymbol{\Pi}_q \mathbf{x}_m = \boldsymbol{\Pi}_q f(\boldsymbol{\tau}_m),\end{aligned} \tag{2}$$

where $\boldsymbol{\Pi}_q \in \mathbb{R}^{P_q\times N}$ is a selection operator that selects the frames in the q-th neighborhood from the whole dynamic image series and $t_p^{(q)} \in \{t_1, \dots, t_N\}, p = 1, \dots, P_q$ denote the time stamps of the selected frames in the q-th neighborhood. The first order Taylor expansion yields the following approximation of the signals in the q-th neighborhood :

$$\mathbf{x}_m^{(q)} \approx \boldsymbol{\Pi}_q f(\bar{\boldsymbol{\tau}}_q) + \boldsymbol{\Pi}_q J_f(\bar{\boldsymbol{\tau}}_q)\,(\boldsymbol{\tau}_m - \bar{\boldsymbol{\tau}}_q), \tag{3}$$

where $\boldsymbol{\Pi}_q f(\bar{\boldsymbol{\tau}}_q)$ is the centroid of the signals in the q-th neighborhood, $\bar{\boldsymbol{\tau}}_q$ is the corresponding coordinate in the feature space, and $\mathbf{J}_f(\cdot) \in \mathbb{C}^{N\times D}$ denotes the Jacobian matrix of f.

On the other hand, the signals in the q-th neighborhood can be expressed by a local Casorati matrix $\mathbf{X}_q \in \mathbb{C}^{M\times P_q}$ as:

$$\mathbf{X}_q = \begin{bmatrix} x(\boldsymbol{r}_1, t_1^{(q)}) & \cdots & x(\boldsymbol{r}_1, t_{P_q}^{(q)}) \\ \vdots & \ddots & \vdots \\ x(\boldsymbol{r}_M, t_1^{(q)}) & \cdots & x(\boldsymbol{r}_M, t_{P_q}^{(q)}) \end{bmatrix}. \tag{4}$$

As in the LR model, the Casorati matrix $\mathbf{X}_q$ can be approximated by a $(D+1)$-dimensional subspace:

$$\mathbf{X}_q = \boldsymbol{\Theta}_q \boldsymbol{\Phi}_q^{\mathrm{T}} \tag{5}$$

where the columns of $\boldsymbol{\Phi}_q \in \mathbb{C}^{P_q\times(D+1)}$ are the temporal bases spanning the subspace and $\boldsymbol{\Theta}_q \in \mathbb{C}^{M\times(D+1)}$ denotes the corresponding local coordinates.

With additional assumptions regarding smoothness and regularity of the underlying manifold and by combining Eq. (3) and Eq. (5), we obtain the following linear tangent space alignment model [17, 18]:

$$\mathbf{X} = \sum_{q=1}^{Q} \mathbf{X}_q \boldsymbol{\Pi}_q = \sum_{q=1}^{Q} \mathbf{T}\mathbf{L}_q \boldsymbol{\Phi}_q^{\mathrm{T}} \boldsymbol{\Pi}_q, \tag{6}$$

where $\mathbf{X}$ denotes the Casorati matrix formed by the entire dynamic image series, $\mathbf{T} \in \mathbb{C}^{M\times(D+1)}$ denotes the augmented global coordinates of the manifold, and $\mathbf{L}_q \in \mathbb{C}^{(D+1)\times(D+1)}, q = 1, \dots, Q$ denote the linear transform matrices that align the local coordinates to the global ones.

2.2. LTSA-based image reconstruction with sparsity constraints

We formulate the image reconstruction problems as the following optimization problem:

$$\begin{aligned}\arg\min_{\mathbf{T},\mathbf{L}} \frac{1}{2} \left\| \boldsymbol{\Omega} \left(\mathbf{F}_s \sum_{q=1}^{Q} \mathbf{T}\mathbf{L}_q \boldsymbol{\Phi}_q^{\mathrm{T}} \boldsymbol{\Pi}_q \right) - \boldsymbol{d} \right\|_2^2 + \frac{\mu_T}{2} \|\mathbf{T}\|_F^2 \\ + \frac{\mu_L}{2} \|\mathbf{L}\|_F^2 + \lambda_T \|\boldsymbol{\mathcal{D}}(\mathbf{T}\mathbf{L})\|_1 + \lambda_L \|vec(\mathbf{L})\|_1 ,\end{aligned} \tag{7}$$

where $\mathbf{d}$ denotes the measured data in the (k,t)-space, $\boldsymbol{\Omega}$ a (k,t)-space sampling operator, $\mathbf{F}_s$ the Non-Uniform Fast Fourier Transform (NUFFT) operator [19], $\|\cdot\|_F$ the Frobenius norm, $\boldsymbol{\mathcal{D}}$ the finite difference operator, and $\mathbf{L} = [\mathbf{L}_1, \dots, \mathbf{L}_Q]$. In addition to the data fidelity term, a total variation penalty is added to promote smoothness in the local coordinates. The second and third term of the cost function are ℓ_2-norm regularization, added to improve numerical stability. Finally, a sparsity constraint on the $\mathbf{L}$ matrix is added using the ℓ_1-norm. The cost function in Eq. (7) extends the one used in [17] by enforcing sparse linear transform matrices $\mathbf{L}$, in order to better select the tangent spaces to be aligned, leading to improved reconstructions. The temporal basis $\boldsymbol{\Phi}_q$ can be estimated directly from the acquired data via singular value decomposition (SVD) as in [17].

The non-convex optimization problem in Eq. (7) can be solved using a nested variation of the Alternating Direction Method of Multipliers (ADMM) [20] algorithm as follows, where we use subscripts "out" and "in" to refer to variables of the outer and inner ADMM loops:

$$\begin{aligned}\mathbf{T}^{(k+1)} =& \arg\min_{\mathbf{T}} \frac{1}{2} \left\| \boldsymbol{\Omega} \left(\mathbf{F}_s \sum_{q=1}^{Q} \mathbf{T}\mathbf{L}_q^{(k)} \boldsymbol{\Phi}_q^{\mathrm{T}} \boldsymbol{\Pi}_q \right) - \boldsymbol{d} \right\|_2^2 \\ &+ \frac{\mu_T}{2} \|\mathbf{T}\|_F^2 \\ &+ \frac{\rho_{out}}{2} \|\boldsymbol{\mathcal{D}}(\mathbf{T}\mathbf{L}^{(k)}) - \mathbf{G}_{\mathbf{T}}^{(k)} + \boldsymbol{\eta}_{out}^{(k)}\|_F^2,\end{aligned} \tag{8}$$

$$\begin{aligned}\mathbf{L}^{(k+1)} =& \arg\min_{\mathbf{L}} \frac{1}{2} \left\| \boldsymbol{\Omega} \left(\mathbf{F}_s \sum_{q=1}^{Q} \mathbf{T}^{(k+1)} \mathbf{L}_q \boldsymbol{\Phi}_q^{\mathrm{T}} \boldsymbol{\Pi}_q \right) - \boldsymbol{d} \right\|_2^2 \\ &+ \lambda_L \|vec(\mathbf{L})\|_1 + \frac{\mu_L}{2} \|\mathbf{L}\|_F^2 \\ &+ \frac{\rho_{out}}{2} \|\boldsymbol{\mathcal{D}}(\mathbf{T}^{(k+1)}\mathbf{L}) - \mathbf{G}_{\mathbf{T}}^{(k)} + \boldsymbol{\eta}_{out}^{(k)}\|_F^2,\end{aligned} \tag{9}$$

$$\mathbf{G}_{\mathbf{T}}^{(k+1)} = \boldsymbol{\mathcal{S}}_{\lambda_T/\rho_{out}}(\boldsymbol{\mathcal{D}}(\mathbf{T}^{(k+1)}\mathbf{L}^{(k+1)}) + \boldsymbol{\eta}_{out}^{(k)}), \tag{10}$$

$$\boldsymbol{\eta}_{out}^{(k+1)} = \boldsymbol{\eta}_{out}^{(k)} + \boldsymbol{\mathcal{D}}(\mathbf{T}^{(k+1)}\mathbf{L}^{(k+1)}) - \mathbf{G}_{\mathbf{T}}^{(k+1)}, \tag{11}$$

where $\mathbf{G_T}$ is the augmented Lagrangian split variable, $\boldsymbol{\eta}_{out}$ is the dual variable, ρ_{out} is a scalar relaxation parameter, and $\boldsymbol{\mathcal{S}}_{\lambda_T/\rho_{out}}$ is a soft-thresholding operator with threshold λ_T/ρ_{out}. The optimization problem in Eq. (8) is convex and can be solved using the conjugate gradient method.

The update of $\mathbf{L}$ in Eq. (9) is performed using a nested ADMM, resulting in the following updates:

$$\begin{aligned}\mathbf{L}^{(k+1,l+1)} &= \arg\min_{\mathbf{L}} \frac{1}{2}\left\|\boldsymbol{\Omega}\left(\mathbf{F}_s\sum_{q=1}^{Q}\mathbf{T}^{(k+1)}\mathbf{L}_q\boldsymbol{\Phi}_q^{\mathrm{T}}\boldsymbol{\Pi}_q\right)-\boldsymbol{d}\right\|_2^2 \\ &+\frac{\mu_L}{2}\|\mathbf{L}\|_F^2+\frac{\rho_{in}}{2}\|\mathbf{L}-\mathbf{G}_{\mathbf{L}}^{(k+1,l)}+\boldsymbol{\eta}_{in}^{(k+1,l)}\|_F^2 \\ &+\frac{\rho_{out}}{2}\|\boldsymbol{\mathcal{D}}(\mathbf{T}^{(k+1)}\mathbf{L})-\mathbf{G}_{\mathbf{T}}^{(k)}+\boldsymbol{\eta}_{out}^{(k)}\|_F^2,\end{aligned} \tag{12}$$

$$\mathbf{G}_{\mathbf{L}}^{(k+1,l+1)} = \boldsymbol{\mathcal{S}}_{\lambda_L/\rho_{in}}(\mathbf{L}^{(k+1,l+1)}+\boldsymbol{\eta}_{in}^{(k+1,l)}), \tag{13}$$

$$\boldsymbol{\eta}_{in}^{(k+1,l+1)} = \boldsymbol{\eta}_{in}^{(k+1,l)}+\mathbf{L}^{(k+1,l+1)}-\mathbf{G}_{\mathbf{L}}^{(k+1,l+1)}. \tag{14}$$

The first sub-problem can be readily solved using conjugate gradient while the other updates have a closed-form solution.

2.3. Implementation

The reconstruction algorithm in Section 2.2 was implemented on graphics processing units (GPUs) using Python and the CuPy library [21] with custom kernels implemented using the Compute Unified Device Architecture (CUDA). The solver was based on the SigPy framework [22], and the MMRT package[1] was used to perform NUFFT on GPUs. Reconstructions were preformed on a computing cluster featuring four Tesla V100-SXM2 GPUs, each equipped with 16 GB of memory. Reconstructions were performed coil-by-coil parallelized over the four GPUs and later combined by computing the root-mean-square average of per-coil reconstructions.

3. RESULTS

3.1. Data acquisition

Experiments were performed on four healthy subjects (1 male and 3 females; 43 ± 16 years) under a study protocol approved by the local institutional review board (IRB). A 3T PET/MR scanner (Biograph mMR, Siemens Healthcare, Erlangen, Germany) was used for imaging with a body coil for transmission and spine and surface coils for reception. Cardiac T_1 mapping was performed before and 10 minutes after the administration of contrast agent (0.1 mmol/kg of Dotarem) using a 3D, free-breathing, ECG-gated, FLASH sequence with $10-(3)-10-(3)$ protocol and sparse sampling along a stack-of-stars trajectory [7]. The imaging parameters were: field-of-view (FOV) = $308 \times 308 \times 144$ mm^3, spatial resolution = $1.9 \times 1.9 \times 4.5$ mm^3, TR/TE = $4.2/1.7$ ms, FA = 9°, inversion delay times = $100/180$ ms, acquisition window per frame = 138.6 ms, and total number of frames = 900 which corresponds to an imaging time of 14.3 ± 2.3 min and 12.7 ± 2.4 min for pre- and post-contrast acquisitions, respectively.

3.2. Image reconstruction results

Throughout the rest of this paper, we refer to the original formulation of the LTSA method (with $\lambda_L = 0$ in Eq. (7)) as LTSA and the proposed method ($\lambda_L > 0$) as sparse-LTSA (sLTSA). Fig. 1 shows the results from the proposed method in comparison with those from the LTSA method and the LR method with a TV-sparsity penalty to promote piece-wise smoothness of the reconstructed images (LR+S) as in [23]. Table 1 summarizes the parameters employed for the reconstructions. The same set of parameters was used across all subjects, demonstrating robust performance across the subjects.

	LTSA	sLTSA
μ_T	1e-5	1e-5
μ_L	1e-10	1e-10
λ_T	1e-10	1e-10
λ_L	0	1e-12
ρ_{out}	0.0001	0.0001
ρ_{in}		1e-8

Table 1. Hyper-parameters used for the LTSA-based image reconstructions.

While all three methods yield reasonable reconstructions, the sLTSA method better mitigated the aliasing artifacts arising from undersampling compared to the other methods (as indicated by red arrows in the middle row of Fig. 1). Specifically within the cardiac region, the myocardium wall in the images reconstructed by the sLSTA method appeared sharper when compared to the LR or the LTSA method (yellow arrows in the middle and bottom row of Fig. 1).

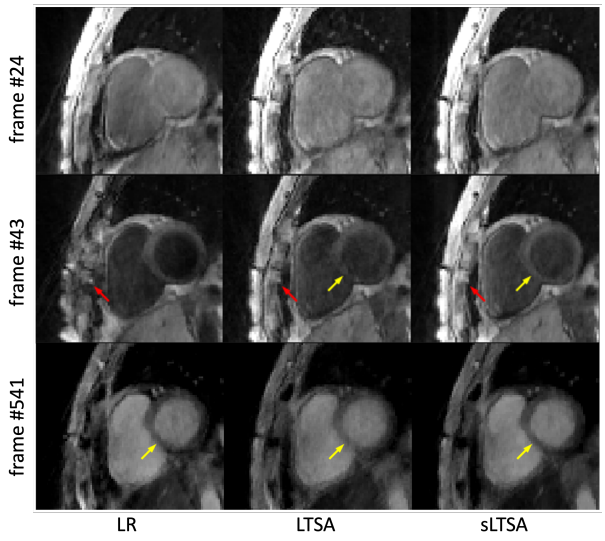

Fig. 1. Representative reconstructed frames using: the LR (left column), the original LTSA (middle column) and the proposed sLTSA (right column) methods.

3.3. T_1 and ECV mapping results

Joint T_1/B_1 mapping was performed as described in [24], on the LR, LTSA and sLTSA reconstructions. The variable projection method was used to isolate the nonlinear components of the model. Basis functions were synthesized using the Bloch equation simulation on a grid of T_1 and B_1 values. For each respiratory phase, voxel-by-voxel fitting was performed to select the T_1/B_1 pair that best fitted the data. As T_1 values vary over time in the post-contrast acquisition,

[1] available at https://github.com/mritools/mrrt.nufft

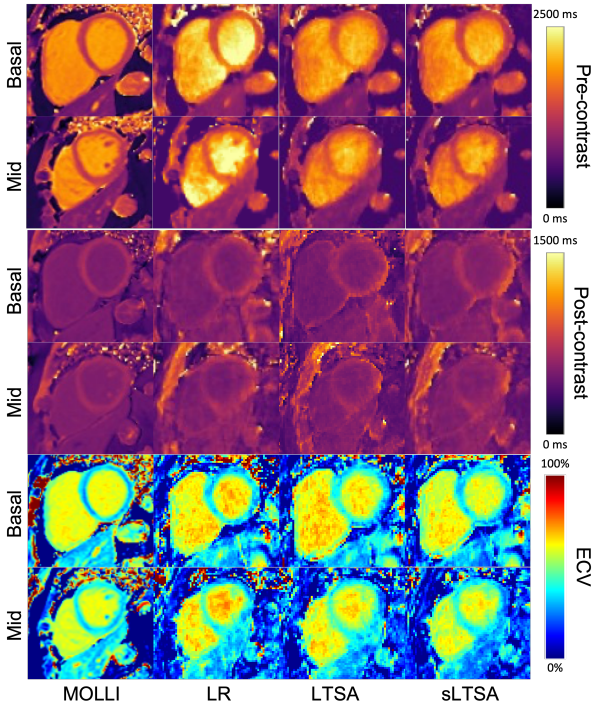

Fig. 2. T_1 maps obtained via MOLLI acquisition (left) compared to different methods: LR (second column), LTSA (third column) and sLTSA (fourth column) shown for basal and mid-ventricular slices for the pre- and post-contrast injection. Last two rows are the corresponding ECV maps with a *HCT* of 40.9% measured from blood samples.

a linear T_1 evolution model was assumed and an additional T_1 rate of change variable was incorporated in the basis functions and the grid search for post-contrast T_1 mapping.

ECV maps were derived from estimated pre- and post-contrast T_1 maps [1]:

$$ECV(\boldsymbol{r}) = (1-HCT)\times \frac{\frac{1}{\textit{post-contrast } T_1(\boldsymbol{r})} - \frac{1}{\textit{pre-contrast } T_1(\boldsymbol{r})}}{\frac{1}{\textit{post-contrast } T_1 \textit{ blood}} - \frac{1}{\textit{pre-contrast } T_1 \textit{ blood}}}, \quad (15)$$

where *HCT* represents the hematocrit value, a measure between 0 and 1, indicating the proportion of red blood cells in the subject's blood and determined through a blood sample, and $\boldsymbol{r}$ is the position in the spatial domain after affine registration was performed to align pre- and post-contrast T_1 maps.

Fig. 2 shows the representative pre- and post-contrast T_1 maps as well as ECV maps obtained by the LR, LTSA, and sLTSA, respectively. The results obtained by the MOLLI method in the same slice positions acquired with breath-holding are also shown as reference. ECV maps obtained from the proposed method display reduced artifacts in the intracavitary blood pool compared to LR and LTSA. Fig. 3 shows the mean and standard deviation of the estimated T_1 values in the intracavitary blood pool and myocardium for the compared methods. As can be seen, the pre-contrast T_1 maps obtained by the LR method overestimated the T_1 values of both myocardium and blood pool both qualitatively as shown in Fig. 2 and quantitatively as shown in Fig. 3. Compared to the LR method, the LTSA and sLTSA methods produced more accurate pre- and post-contrast

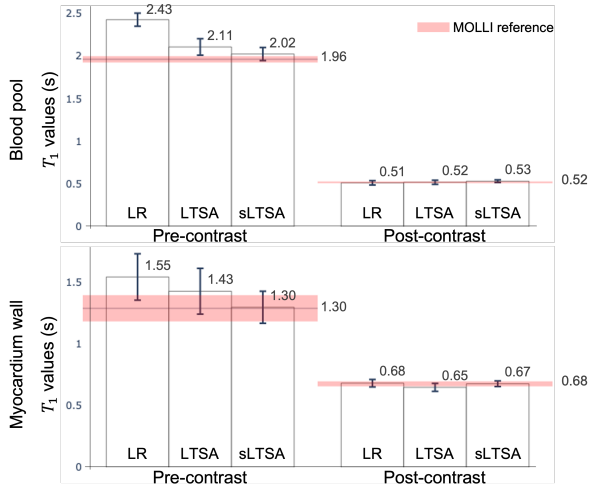

Fig. 3. T_1 values from the mid-ventricular slice in the intracavitary blood pool and myocardium. Horizontal lines correspond to the MOLLI reference. Error bars indicate the standard deviation in the region.

T_1 maps that are in good agreement with MOLLI. Compared to the LTSA method, the additional sparsity constraint in the sLSTA method further improved the quality of the reconstructed parametric maps. Notably, the myocardium walls in the pre-contrast T_1 and ECV maps obtained by the sLTSA method were better defined than those by the LTSA method.

4. CONCLUSION

This work presents a sparsity constrained Linear Tangent Space Alignment (sLTSA) model for free-breathing 3D cardiac T_1 mapping. The performance of the proposed method is validated using in vivo MR data acquired from healthy subjects at 3T. The proposed method produced pre- and post-contrast T_1 maps and ECV maps in good agreement with the reference 2D MOLLI method and showed superior performance both qualitative and quantitatively when compared to the Low-Rank method and the original LTSA method.

5. COMPLIANCE WITH ETHICAL STANDARDS

The experiments performed in this study were approved by the local institutional review board (IRB) at Massachusetts General Hospital and all subjects provided informed consent. The research was conducted in accordance with the principles embodied in the Declaration of Helsinki and in accordance with local statutory requirements.

6. ACKNOWLEDGMENTS AND FUNDING

This work was supported in part by the National Institutes of Health under the grants P41EB022544, R01EB033582, R01CA165221, R01HL137230, K01EB030045, and T32EB013180.

7. REFERENCES

[1] P. Haaf et al. “Cardiac T1 Mapping and Extracellular Volume (ECV) in clinical practice: a comprehensive review”. In: *Journal of Cardiovascular Magnetic Resonance* 18.1 (Nov. 2016), p. 89.

[2] D. R. Messroghli et al. “Clinical recommendations for cardiovascular magnetic resonance mapping of T1, T2, T2* and extracellular volume: A consensus statement by the Society for Cardiovascular Magnetic Resonance (SCMR) endorsed by the European Association for Cardiovascular Imaging (EACVI)”. In: *Journal of Cardiovascular Magnetic Resonance* 19.1 (Oct. 2017), p. 75.

[3] D. R. Messroghli et al. “Modified Look-Locker inversion recovery (MOLLI) for high-resolution T1 mapping of the heart”. In: *Magnetic Resonance in Medicine* 52.1 (2004), pp. 141–146.

[4] S. Weingärtner et al. “Simultaneous multislice imaging for native myocardial T $_1$ mapping: Improved spatial coverage in a single breath-hold: Multislice Imaging for Myocardial T $_1$ Mapping”. en. In: *Magnetic Resonance in Medicine* 78.2 (Aug. 2017), pp. 462–471.

[5] Y. Chen et al. “Single breath-hold 3D cardiac T_1 mapping using through-time spiral GRAPPA”. en. In: *NMR in Biomedicine* 31.6 (June 2018), e3923.

[6] Z.-P. Liang. “Spatiotemporal Imaging with Partially Separable Functions”. In: *IEEE International Symposium on Biomedical Imaging*. 2007 4th IEEE International Symposium on Biomedical Imaging: From Nano to Macro. 2007, pp. 988–991.

[7] P. K. Han et al. “Free-breathing 3D cardiac T $_1$ mapping with transmit B $_1$ correction at 3T”. en. In: *Magnetic Resonance in Medicine* 87.4 (Apr. 2022), pp. 1832–1845.

[8] J. D. Trzasko. “Exploiting local low-rank structure in higher-dimensional MRI applications”. In: *Wavelets and Sparsity XV*. Vol. 8858. SPIE, Sept. 2013, pp. 551–558.

[9] J. Trzasko, A. Manduca, and E. Borisch. “Local versus global low-rank promotion in dynamic MRI series reconstruction”. In: *Proc. Int. Symp. Magn. Reson. Med.* (Jan. 2011).

[10] F. Ong et al. “Extreme MRI: Large-scale volumetric dynamic imaging from continuous non-gated acquisitions”. en. In: *Magnetic Resonance in Medicine* 84.4 (2020), pp. 1763–1780.

[11] J. He et al. “Accelerated High-Dimensional MR Imaging With Sparse Sampling Using Low-Rank Tensors”. In: *IEEE Transactions on Medical Imaging* 35.9 (Sept. 2016), pp. 2119–2129.

[12] A. G. Christodoulou et al. “Magnetic resonance multitasking for motion-resolved quantitative cardiovascular imaging”. en. In: *Nature Biomedical Engineering* 2.4 (Apr. 2018), pp. 215–226.

[13] J. L. Shaw et al. “Free-breathing, non-ECG, continuous myocardial T1 mapping with cardiovascular magnetic resonance multitasking”. English. In: *Magnetic Resonance in Medicine* 81.4 (2019), pp. 2450–2463.

[14] H. Qi et al. “Free-running 3D whole heart myocardial T1 mapping with isotropic spatial resolution”. English. In: *Magnetic Resonance in Medicine* 82.4 (2019), pp. 1331–1342.

[15] R. Guo et al. “Accelerated cardiac T1 mapping in four heartbeats with inline MyoMapNet: a deep learning-based T1 estimation approach”. In: *Journal of Cardiovascular Magnetic Resonance* 24.1 (Jan. 2022), p. 6.

[16] J. I. Hamilton et al. “Deep learning reconstruction for cardiac magnetic resonance fingerprinting T1 and T2 mapping”. eng. In: *Magnetic Resonance in Medicine* 85.4 (Apr. 2021), pp. 2127–2135.

[17] Y. Djebra et al. “Manifold Learning via Linear Tangent Space Alignment (LTSA) for Accelerated Dynamic MRI With Sparse Sampling”. In: *IEEE Transactions on Medical Imaging* 42.1 (Jan. 2023), pp. 158–169.

[18] C. Ma et al. “Joint spectral quantification of MR spectroscopic imaging using linear tangent space alignment (LTSA)-based manifold learning”. In: *Magnetic resonance in medicine* 89.4 (Apr. 2023), pp. 1297–1313.

[19] J. Fessler and B. Sutton. “Nonuniform fast fourier transforms using min-max interpolation”. en. In: *IEEE Trans. Signal Process.* 51.2 (Feb. 2003), pp. 560–574.

[20] S. Boyd et al. “Distributed Optimization and Statistical Learning via the Alternating Direction Method of Multipliers”. In: *Foundations and Trends in Machine Learning* 3.1 (2011), pp. 1–122.

[21] R. Okuta et al. “Cupy: A NumPy-compatible library for NVIDIA GPU calculations”. In: *International Conference on Neural Information Processing Systems*. Vol. 6. 2017.

[22] F. Ong and M. Lustig. “SigPy: A Python Package for High Performance Iterative Reconstruction”. In: *Proc. ISMRM*. 2019.

[23] T. Marin et al. “Motion correction for PET data using subspace-based real-time MR imaging in simultaneous PET/MR”. en. In: *Phys. Med. Biol.* 65.23 (Dec. 2020), p. 235022.

[24] P. K. Han et al. “Free-Breathing Three-Dimensional T $_1$ Mapping of the Heart Using Subspace-Based Data Acquisition and Image Reconstruction”. en. In: *2019 41st Annual International Conference of the IEEE Engineering in Medicine and Biology Society (EMBC)*. Berlin, Germany: IEEE, July 2019, pp. 4008–4011.